ARTICLE

Silver-Based Nanodisk Codes

Matthew J. Banholzer,[†,§,⊥] Kyle D. Osberg,[‡,§,⊥] Shuzhou Li,[†,§] Bryan F. Mangelson,[†,§] George C. Schatz,[†,§] and Chad A. Mirkin*[,†,‡,§]

[†]Department of Chemistry, [‡]Department of Materials Science and Engineering, and [§]International Institute of Nanotechnology, Northwestern University, Evanston, Illinois 60208-3113. [⊥]These authors contributed equally to this work.

ABSTRACT We report a novel method for synthesizing silver-based nanodisk code (NDC) structures using on-wire lithography, where we employ milder synthetic and etching conditions than those used to synthesize the analogous gold structures. The silver structures exhibit stronger surface-enhanced Raman scattering signals than their Au counterparts at 633 and 532 nm excitation and, therefore, lead to lower limits of detection when used in the context of DNA-based detection assays. Finally, use of two enhancing nanostructured materials in one disk code dramatically increases the information storage density for encoding. For example, a disk code consisting of 5 gold disk pairs has 13 unique combinations of enhancing patterns, while one with 5 disk pairs that can be either gold or silver has 98.

KEYWORDS: encoding · tagging · surface-enhanced Raman scattering · SERS · on-wire lithography · biodetection

Covert encoding and tracking are becoming increasingly important for a variety of applications and industries, including authentication in anticounterfeiting strategies,[1,2] materials and personnel tracking,[3] and in chemical and biological detection.[1,3−12] Nanostructures are an ideal choice for these encoding materials because they can be incorporated into many media without substantively changing their macroscopic appearances and have properties that can be rationally and deliberately tailored in a variety of ways.[1,6,13−28] Among the structures that have been studied to date, striped nanowires show significant promise both in terms of fundamental studies and commercial applications.[20,21]

Recently, our group reported a novel nanoscale encoding system based upon dispersible and highly tailorable linear arrays of Au nanodisk pairs generated by on-wire lithography (OWL) and functionalized with Raman chromophores.[1,14,17,29] With these structures, termed nanodisk codes (NDCs), each disk pair is a surface-enhanced Raman scattering (SERS) hotspot that produces a large Raman signal when scanned with a confocal Raman microscope, representing a "1" in the physical binary readout.[1] Alternatively, the absence of a disk pair and its corresponding signal along the array represents a "0". Thus, information is stored based on the number and the relative location of disk pairs along the array. In addition, the spectroscopic fingerprint of the adsorbed Raman chromophores provides an additional level of chemical information storage. The geometry and dimensions of the disk structures utilized were optimized based upon previous structure−function studies,[17] and the high degree of tailorability afforded by OWL in the number and spacing of the disk pairs creates many unique code permutations. In principle, these structures can be used to create a library of encoded labels that may be useful in anticounterfeiting and biodiagnostics.[1]

Thus far, work with nanodisk codes has involved structures consisting only of gold; however, analogous silver or mixed gold−silver NDC structures may exhibit properties that could further increase their scope of application. For example, silver, in principle, should lead to larger enhancements than the gold structures, while also providing additional available excitation wavelengths with large enhancements.[30] Furthermore, greater degrees of information storage may be possible, since information content would now correlate with the metallic composition of each hotspot, in addition to the number, position, and spectroscopic signature of chromophores used to functionalize them. Herein, we report the first synthesis and characterization of Ag nanodisk code structures with optimized and improved (compared to the gold system) optical properties for encoding and

*Address correspondence to chadnano@northwestern.edu

Received for review June 1, 2010 and accepted July 28, 2010.

Published online August 5, 2010. 10.1021/nn101231u

© 2010 American Chemical Society

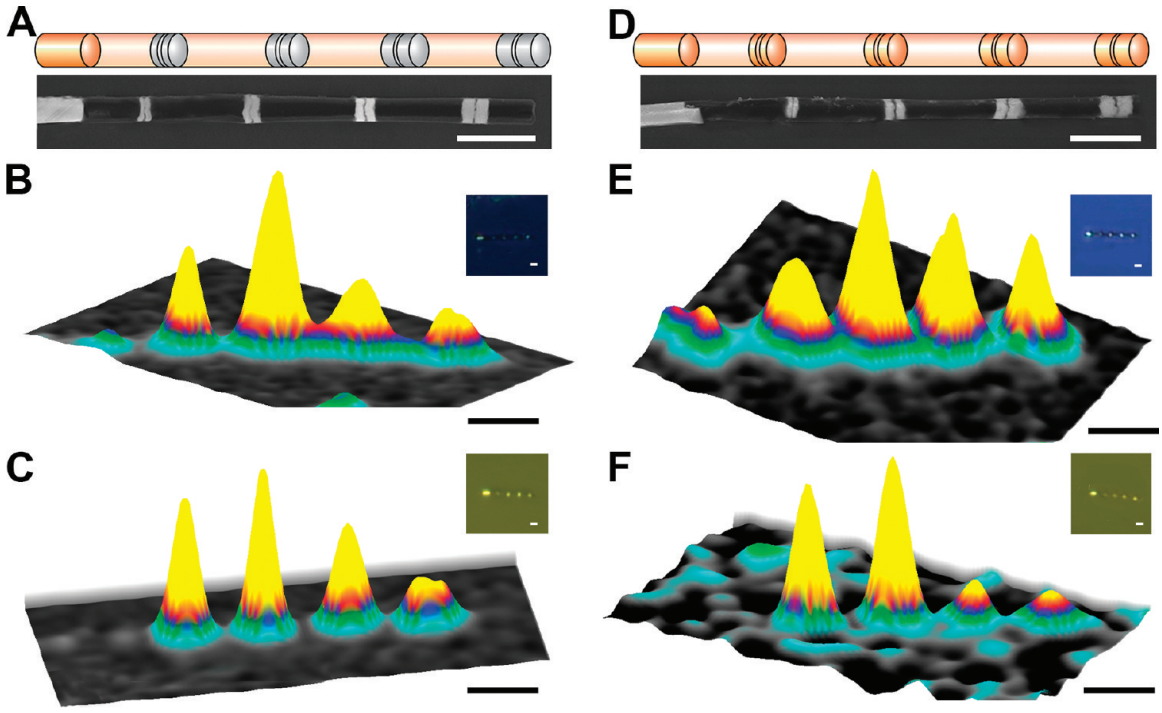

Figure 1. Effect of varying disk thickness on SERS enhancement for Ag (A−C) and Au (D−F) nanodisk dimers at λ_{ex} = 532 and 632 nm. (A) Schematic and SEM image of the Ag test array structure made up of disk dimers with 30 nm gaps and disk thicknesses of (left to right) 60, 90, 120, and 150 nm. Adjacent disk pairs are spaced by 1 μm. (B and C) Representative Raman maps of integrated intensity at 633 (B) and 532 nm (C) excitation wavelengths. At both wavelengths, the 90 nm disk dimers are the most enhancing, followed by 60, 120, and 150 nm dimers. Insets depict optical images of each nanostructure. (D−F) Similar to A−C but for Au instead of Ag. (D) Schematic and SEM image of Au test array structure made up of disk dimers with 30 nm gaps and disk thicknesses of (left to right) 60, 90, 120, and 150 nm. Adjacent disk pairs are spaced by 1 μm. (E and F) Representative Raman maps of integrated intensity at 633 (E) and 532 nm (F) excitation wavelengths. Again, at both wavelengths, the 90 nm disk dimers are the most enhancing, followed by 60, 120, and 150 nm dimers. Insets depict optical images of each nanostructure. All scale bars are 1 μm. Au ends were used in both cases to provide a means of distinguishing the two nanorod ends in the optical images (insets).

sensing platforms. Notably, we find that Ag-based systems have stronger enhancements at both 633 and 532 nm excitation wavelengths, with particularly large increases observed at 532 nm, allowing for stronger signals and lower detection limits. Additionally, we find that we can take advantage of the large difference in SERS signals from the two metals to produce NDCs with added functionality and increased encoding sophistication through a new multicomponent encoding scheme.

RESULTS AND DISCUSSION

A series of structure−function studies were carried out with the Ag NDCs to tune the surface plasmon resonances (SPRs) of the nanostructures so that they are resonant with λ_{ex}. This allows one to determine the ideal geometry of the disk pairs to achieve maximum SERS enhancement in a manner similar to the Au NDCs.[17] The geometry components of interest (disk and gap size) affect the enhancement of the ensemble structures in different and complex ways and must be reoptimized for new materials and excitation wavelengths. Therefore, using the previous Au studies as a starting point,[17] both Au and Ag structures with a range of disk and gap sizes were synthesized, functionalized with *para*-mercapto aniline (PMA), and studied using confocal Raman microscopy to compare their relative SERS enhancements at λ_{ex} = 633 and 532 nm. While Au structures had been previously optimized at 633 nm, they were reoptimized in this work because the nanostructures described here have a significantly smaller diameter than those previously studied (273 nm instead of 360 nm). The smaller diameter structures are easier to synthesize (the larger diameter structures are made from templates that often result in nanowires that are connected and difficult to disperse) and, in principle, should lead to larger SERS enhancements.[30]

As a first step, we carried out discrete dipole approximation (DDA) calculations to determine the theoretical electromagnetic field enhancements for Au and Ag dimers with varying gap sizes and disk lengths.[31] Maxima were observed for structures with approximately 90 nm disks and 12 nm gaps, providing a guide for the OWL-based synthesis. Since these results are similar to those for Au, where the experimental optimum gap thickness was determined to be 30 nm instead of the predicted 10 nm due to surface roughness, experiments were designed to focus on structures with disk lengths ranging from 60 and 150 nm and gap thick-

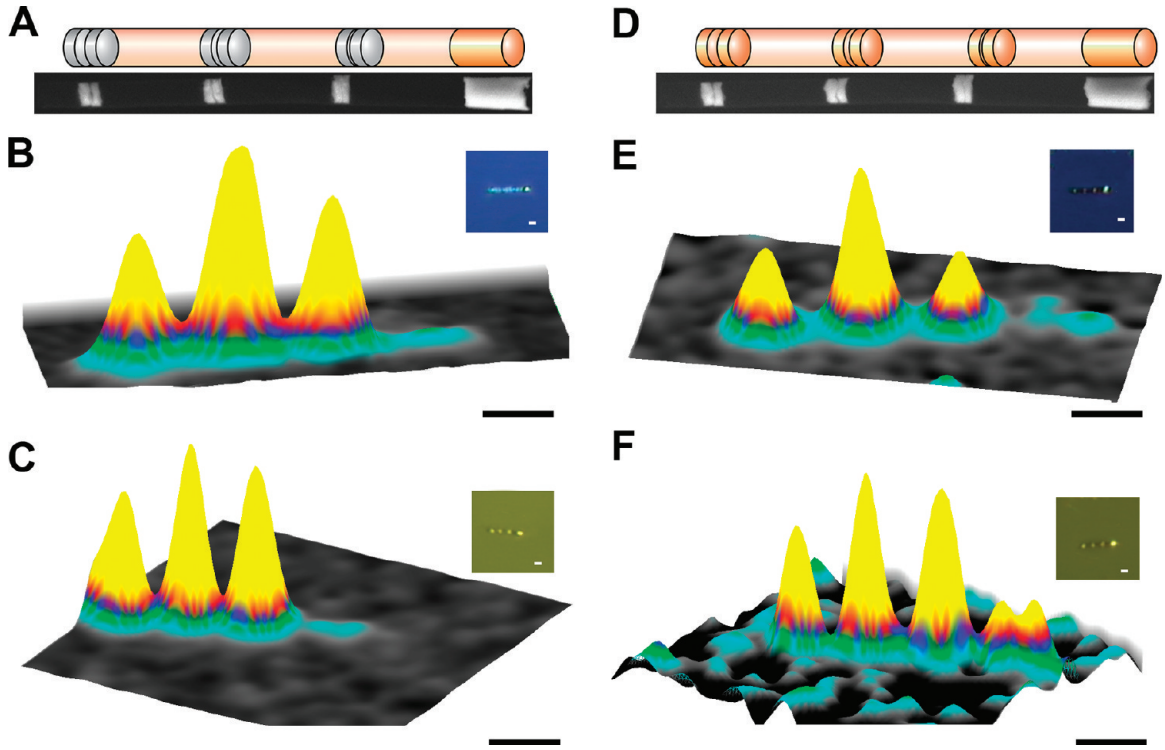

Figure 2. Effect of varying gap thickness on SERS enhancement for Ag (left) and Au (right) nanodisk dimers at λ_{ex} = 532 and 632 nm. (A) Schematic and SEM image of Ag test array structure made up of disk dimers with 90 nm gaps and gap thicknesses of (left to right) 15, 30, and 45 nm. Adjacent disk pairs are spaced by 1 μm. (B and C) Representative Raman maps of integrated intensity at (B) 633 and (C) 532 nm excitation. At both wavelengths, 30 nm gaps are the most enhancing, followed by 15 and 45 nm. (D−F) Similar to A−C but for Au instead of Ag. (D) Schematic and SEM image of Au test array structure made up of disk dimers with 90 nm gaps and gap thicknesses of (left to right) 15, 30, and 45 nm. Adjacent disk pairs are spaced by 1 μm. (E and F) Representative Raman maps of integrated intensity at (E) 633 and (F) 532 nm excitations. Again, at both wavelengths, 30 nm gaps are the most enhancing, followed by 15 and 45 nm. Insets depict optical images of each nanostructure. All scale bars are 1 μm. Au ends were used in both cases to provide a means of distinguishing the two nanorod ends in the optical images (insets).

nesses ranging from 15 to 45 nm for both Au and Ag.[17,32,33] The computationally predicted values were the midpoints for both of these ranges.

For determining the optimum disk sizes, Au and Ag test structures consisting of arrays of dimers, each with 30 nm gaps and varying disk thicknesses of 60, 90, 120, and 150 nm, were synthesized. Adjacent dimers were separated by 1 μm in order to easily resolve their respective SERS signals (Figure 1). Gaps of 30 nm were chosen for these experiments, because 30 nm was the previously determined optimum for Au structures at 633 nm excitation.[17] For Au and Ag at both excitation wavelengths, the signal from the 90 nm disk pair is the largest, followed by the 60 and 120 nm dimers surrounding it (Figure 1). This trend is highly reproducible across the 10 plus nanowires studied (at each excitation wavelength), with the only exception coming from the 60 nm disk pairs; due to their small size, the 60 nm structures have a greater variation in structure, and imperfections in them can lead to a more variable SERS response. It is important to note that each of the Raman intensity maps in Figures 1 and 2 have different intensity scales, and therefore, one can only extract quantitative comparative data within a single nanostructure (wire). Each of the images shown is representative of the response observed for the 10 or more structures studied in each sample set. The longer Au segment on one end of the structures was deliberately designed and included to serve as an optical tag for differentiating the two ends of the rods in the optical images (insets of Figures 1−3). A representative SERS spectrum of PMA from this study is shown in the Supporting Information (Figure S1).

Raman response as a function of gap size was studied in a similar manner. The structures evaluated consisted of 90 nm disks separated by gaps of 15, 30, and 45 nm, respectively (Figure 2). For both Au and Ag at 633 and 532 nm excitation wavelengths, 30 nm gaps produce the maximum Raman signal, followed by the 15 nm structures (Figure 2). From the analysis of Figures 1 and 2, we can say that Au and Ag disk dimers comprised of 90 nm disks spaced by 30 nm gaps are the optimum geometries to produce maximum SERS signals at both 633 and 532 nm excitation wavelengths. This result agrees well with previous experimental work for Au at 633 nm, where deviations from the 120 nm disks and 30 nm gaps found in that study can easily be explained by changes in material, excitation wavelength,

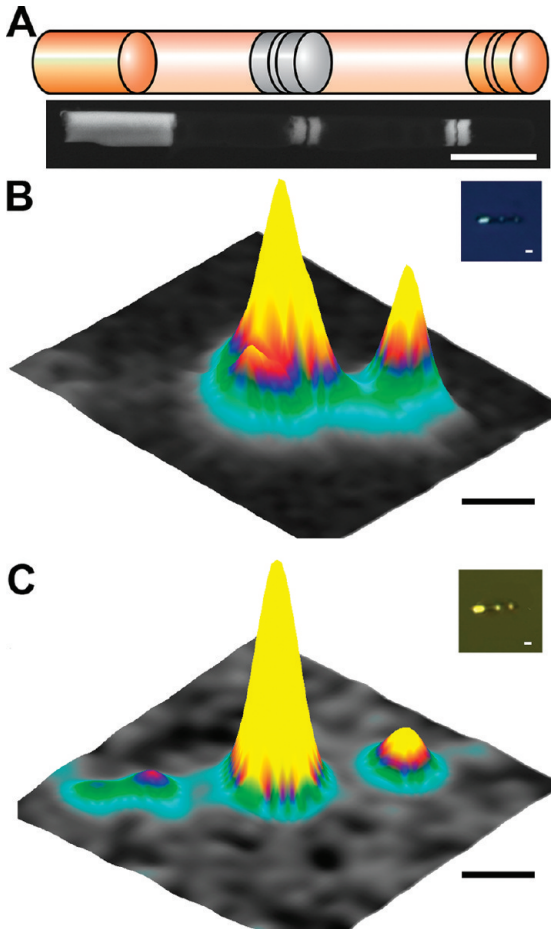

Figure 3. Direct comparison between optimized Ag and Au nanodisk dimers. (A) Schematic and SEM image of a comparison structure with an optimized Ag disk dimer on the left and an optimized Au disk pair on the right. Both structures consist of 90 nm disks separated by 30 nm gaps. (B and C) Representative integrated Raman intensity maps of the comparison structure at 633 (B) and 532 nm (C) excitation. In both cases, Ag has a significantly larger signal than Au: 4.4 times larger at 633 nm and 9300 times larger at 532 nm. Insets depict optical images of each nanostructure. Scale bars are all 1 μm.

and nanowire diameter discussed previously. To understand and compare the optical properties of this structure to that of the Au system, we calculated the extinction spectrum of the optimized Ag dimer (90 nm disks spaced by a 12 nm gap for theory) and observed resonance peaks around 633 and 532 nm, respectively, explaining the high signals at both wavelengths (Supporting Information Figure S2). Au has similar resonance peaks around 632 nm but significantly lower extinction at 532 nm, highlighting the importance of expanding the versatility of the NDC system with Ag.

After independently investigating the geometries of Au and Ag at both wavelengths, we designed and synthesized test structures to directly compare their relative enhancing capabilities by placing optimum Au and Ag dimers (90 nm disks with 30 nm gaps) within the same wire structure (Figure 3A). After functionalizing with PMA, the structures were compared by Raman

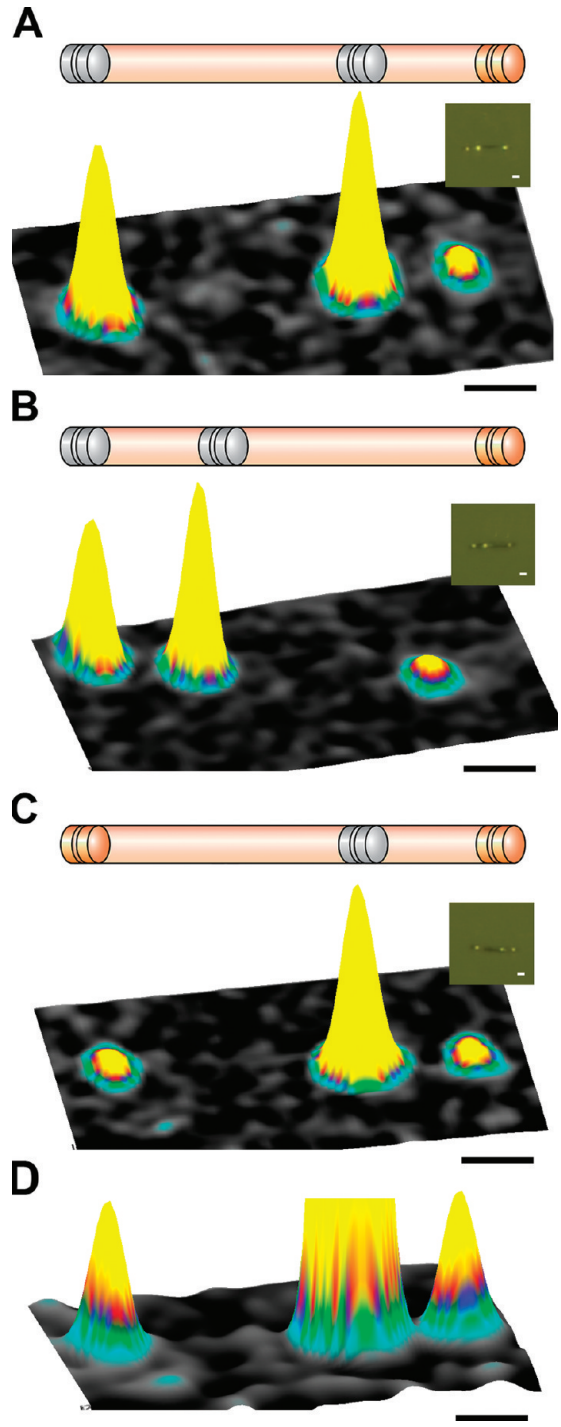

Figure 4. Trinary encoding scheme for hybrid Ag−Au NDCs. In each case, the larger enhancement of Ag dimers corresponds to a value of "2", the smaller enhancement of Au dimers corresponds to a value of "1", and areas intentionally left blank correspond to a value of "0". (A−C) Schemes and representative integrated Raman intensity maps for three example codes: (A) 2021, (B) 2201, and (C) 1021. (D) Magnified image of the 1021 code in (C), illustrating that the signal from the less enhancing Au dimers is easily distinguished from the background signal. All experiments involved 532 nm excitation. Insets are optical images of each nanostructure. Scale bars are all 1 μm.

microscopy at both 633 (Figure 3B) and 532 nm excitation (Figure 3C). Not surprisingly, Ag was found to have

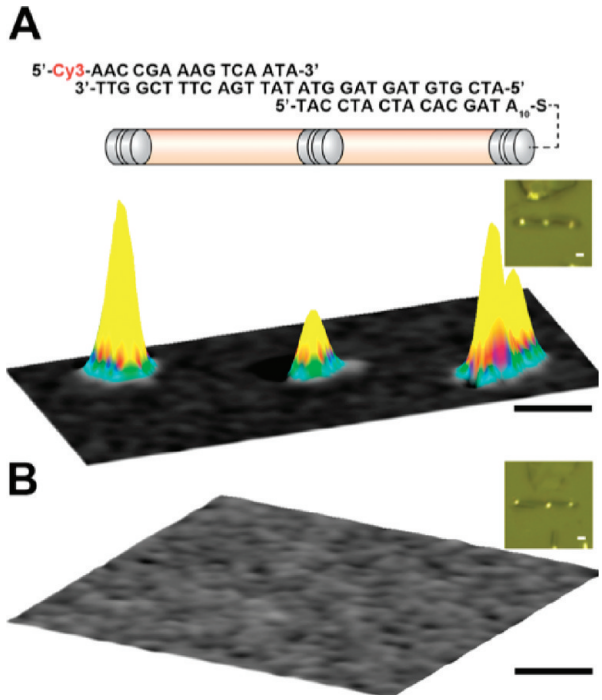

Figure 5. Demonstration of ssDNA detection capabilities of Ag NDC dimers using a three-strand assay. (A) Schematic and representative integrated Raman intensity map for the case of 500 fM target concentration, illustrating an order of magnitude improvement from the previous Au system. (B) Integrated Raman intensity map of the control experiment without target but with the other strands present. Insets are optical images of each nanostructure. (A) and (B) are set to the same *z*-scale for comparison purposes. Scale bars are all 1 μm.

significantly larger SERS signals than Au at both wavelengths. At 633 nm, the average integrated signal intensity from the Ag structure was 4.4 times larger than Au. At 532 nm, the average difference is increased significantly to 9.3×10^3 times, which results from both larger Ag signals and an obvious decrease in the Au signal compared to 633 nm due to plasmon dampening in Au at shorter wavelengths.[30,34,35] Indeed, this large reduction in signal intensity for Au at 532 nm also can be observed in the lower signal-to-noise results in Figures 1F and 2D. These results are not surprising; extinction spectra of these dimers indicate that Ag is much more strongly resonant than Au at 532 nm excitation (Supporting Information, Figure S2). These improvements afforded by Ag have two important consequences: better signal-to-noise, which can lead to more sensitive detection, and increased versatility in terms of choice of excitation wavelength. This second observation is important since 532 nm lasers are commonly used in the SERS community.

In addition to providing a more versatile and powerful SERS material, Ag also can be harnessed to extend the sophistication of NDCs. By utilizing the large difference in signal intensity between Au and Ag at 532 nm excitation (Figure 3C), we designed a trinary encoding system where the larger signal from Ag structures adds an additional possibility to each digit location. Thus, the absence of a disk pair and the presence of a Au disk pair still equate to a "0" and a "1", respectively, but Ag disk pairs, which exhibit a 3 orders of magnitude larger signal now become a "2", greatly increasing the sophistication of the encoding system and the density of stored information. As a proof-of-concept, we synthesized and measured three unique codes at 532 nm excitation: 2021, 2201, and 1021 (Figure 4). In each case, the large difference in signals between Ag and Au is apparent and easily distinguishable. While Au signals are weaker, they are still easily observed above background; this is shown in Figure 4D, which contains a magnified version of Figure 4C. With an additional choice at each of the locations along the array, the number of unique codes available increases dramatically (Supporting Information, Table S1). For example, with five coding digits (*i.e.*, 10101), the previously reported Au binary system could yield 13 unique codes,[1] whereas the Au−Ag trinary system leads to 98 unique possible codes. As the number of possible disk pairs increases to 10, the number of codes becomes 19 925 (Supporting Information, Table S1).

The use of NDCs for biological assays was previously studied in the context of the pure Au system.[1] To quantify how the measured improvements with Ag translate to increased detection sensitivity, the same DNA detection assay that was utilized for the initial Au NDC was studied in the context of the pure Ag system. In these experiments, we employed a three-strand "sandwich" assay where thiol-modified single-stranded oligonucleotides (ssDNA) were attached to the Ag surfaces of a 20202 NDC using literature procedures.[14] These strands contained a sequence complementary to one-half of the target ssDNA sequence (see Supporting Information for sequences used). The remaining half of the target sequence is complementary to a reporter strand that contains a Raman-active probe, Cy3. Because the disk pairs generate a high SERS enhancement, even a small number of binding events can be detected by Raman microscopy on the NDCs. Using the same conditions and DNA sequences, the previous Au system was able to detect the target strand down to a limit of detection (LOD) of 5 pM.[1] With the enhanced sensitivity of the Ag structures, we are able to detect DNA down to a LOD of 500 fM (Figure 5A). Importantly, there is no detectable Raman signal from any of the Ag disk pair locations for the control experiment without target present (Figure 5B). A representative Raman spectrum of the Cy3 tag from the 500 fM detection can be found in Supporting Information Figure S3.

In conclusion, we report the synthesis and characterization of novel Ag-based NDCs. These structures ex-

hibit larger SERS enhancements than their Au counterparts over a broader range of excitation wavelengths, and when heterostructures consisting of both Au and Ag disk pairs are made, trinary encoding becomes possible. Readout is both wavelength and material dependent, leading to a significant increase in the density of stored information. Additionally, the structures can be used in the context of high sensitivity biological assays with detection of a single-strand DNA target demonstrated down to a LOD of 500 fM.

METHODS

Like their Au counterparts, Ag-based NDCs were prepared by OWL from multisegmented nanowires synthesized electrochemically within anodic aluminum oxide (AAO) templates.[1,14,29,36−38] AAO templates were purchased from GE Healthcare (Whatman Anodisc 47) with a nominal pore diameter of 0.2 μm, resulting in nanowires with an average diameter of 273 nm. A 200 nm thick Ag layer was evaporated on one side of these templates (the "top" side of the templates when received from the manufacturer), and nanowires were electrochemically synthesized with Ag and Au segments and sacrificial Ni regions. Ag segments were deposited at −1150 mV (vs Ag/AgCl reference) in a solution of Ag 1025 RTU (Technic, Inc.) that was diluted 20-fold with an additional 1 g of KCN added per 50 mL of solution. These conditions enable the deposition of high-quality monodisperse Ag segments, while avoiding poor Ag−Ni junctions that commonly form when electrodepositing Ag on Ni electrodes (Supporting Information, Figures S4 and S5). Ni segments that serve to generate gaps between individual Ag or Au disks were deposited at −1000 mV in a solution of nickel sulfamate (Technic, diluted 10-fold from commercial stock). Ni sections that served to generate the spacers between disk pairs were deposited at −930 mV with undiluted nickel sulfamate solution, and Au sections were deposited at −930 mV with Orotemp 24 rack plating solution (Technic). After the electrochemical synthesis procedure, the nanowires were released from the templates by first oxidatively dissolving the evaporated Ag backing layer with a 3:1:1 mixture of 95% ethanol, 30% H_2O_2 in H_2O, and 28% NH_4OH in H_2O. Note that ~500 nm of Ni was typically deposited at both ends of the nanowires in order to protect the interior Ag disk segments from etching during this process. The AAO templates were then dissolved with 3 M NaOH, and the rods were subsequently drop cast on glass slides. A thin SiO_2 film was deposited on the slides by plasma enhanced chemical vapor deposition (PECVD) to provide a support layer on each nanowire. This was carried out at 250 °C, instead of the typical 300 °C, in order to prevent Ag migration into the Ni sections while maintaining high-quality SiO_2 films.[14] After sonication to release the nanowires, the sacrificial Ni layers were etched with 50% H_3PO_4 in H_2O for 1.5 days. H_3PO_4 was used in order to limit damage to Ag segments caused by HCl, which is a more aggressive Ni etchant that has been previously used for Au-based OWL structures.[29] Resulting Ag NDC structures were well formed (disks were always cylindrical and well attached to the continuous and rigid SiO_2 backing layer) with the final control and quality comparable to the Au system (Figures 1 and 2 A and D). To study the physical properties of the nanostructures and to evaluate their potential for encoding, we functionalized them by treating them with a 5 mM ethanolic solution of *p*-mercapto aniline (PMA, Alfa Aesar) for 2 h. NDC structures were subsequently isolated by centrifugation (1500 rpm) and then resuspended in 95% ethanol. To analyze them, a 15 μL aliquot of this suspension was deposited on a glass microscope slide and allowed to dry. For DNA detection studies, functionalization was performed in accordance with previously published procedures.[1,14] In both functionalization schemes, the resulting structures were imaged *via* confocal Raman microscopy with a Witec Alpha 300 system at λ_{ex} = 633 and 532 nm, respectively. At least 12 rods were studied for each experiment, and the standard deviation between samples was less than 10% of the mean value for each sample. Imaging conditions were nearly identical to those reported for previous NDCs. In a given experiment, the 633 or 532 nm laser (330 μW) was focused through an 100× Nikon objective onto a ~1 μm spot.[1,14] Laser power was checked prior to each experiment with either a Thorlabs PM130 slim optical power meter or an in-line power meter.

Acknowledgment. The authors acknowledge Andrew E. Prigodich for helpful discussions in determining the trinary code permutations. C.A.M. acknowledges an NSSEF Fellowship from the DoD, DARPA, and the AFOSR for supporting this work. C.A.M. and G.C.S. are grateful for National Science Foundation (NSF) MRSEC support. M.J.B. and K.D.O. acknowledge Northwestern University for Ryan Fellowships, and K.D.O. also acknowledges the NSF for a Graduate Research Fellowship. S. Li was supported by DARPA.

Supporting Information Available: Additional experimental procedures for the synthesis of monodisperse Ag nanowire segments, representative Raman spectra of samples, theoretical extinction spectra for the optimal Au and Ag dimer structures, and the calculation of the number of unique code structures. This material is available free of charge *via* the Internet at http://pubs.acs.org.

REFERENCES AND NOTES

1. Qin, L.; Banholzer, M. J.; Millstone, J. E.; Mirkin, C. A. Nanodisk Codes. *Nano Lett.* **2007**, *7*, 3849–3853.
2. Piner, R. D.; Zhu, J.; Xu, F.; Hong, S.; Mirkin, C. A. Dip-Pen Nanolithography. *Science* **1999**, *283*, 661–663.
3. Wilson, R.; Cossins, A. R.; Spiller, D. G. Encoded Microcarriers For High-Throughput Multiplexed Detection. *Angew. Chem., Int. Ed.* **2006**, *45*, 6104–6117.
4. Alvarez-Puebla, R. A.; Liz-Marzán, L. M. SERS-Based Diagnosis and Biodetection. *Small* **2010**, *6*, 604–610.
5. Nolan, J. P.; Sklar, L. A. Suspension Array Technology: Evolution of the Flat-Array Paradigm. *Trends Biotechnol.* **2002**, *20*, 9–12.
6. Birtwell, S.; Morgan, H. Microparticle Encoding Technologies for High-Throughput Multiplexed Suspension Assays. *Integr. Biol.* **2009**, *1*, 345–362.
7. Pregibon, D. C.; Toner, M.; Doyle, P. S. Multifunctional Encoded Particles for High-Throughput Biomolecule Analysis. *Science* **2007**, *315*, 1393–1396.
8. Gunderson, K. L.; Kruglyak, S.; Graige, M. S.; Garcia, F.; Kermani, B. G.; Zhao, C.; Che, D.; Dickinson, T.; Wickham, E.; Bierle, J.; et al. Decoding Randomly Ordered DNA Arrays. *Genome Res.* **2007**, *14*, 870–877.
9. Kang, T.; Yoo, S. M.; Yoon, I.; Lee, S. Y.; Kim, B. Patterned Multiplex Pathogen DNA Detection by Au Particle-on-Wire SERS Sensor. *Nano Lett.* **2010**, *10*, 1189–1193.
10. Fernandez-Rosas, E.; Gómez, R.; Ibañez, E.; Barrios, L.; Duch, M.; Esteve, J.; Nogués, C.; Plaza, J. A. Intracellular Polysilicon Barcodes for Cell Tracking. *Small* **2009**, *5*, 2433–2439.
11. Jeon, J.; Lim, D.-K.; Nam, J.-M. Functional Nanomaterial-Based Amplified Bio-Detection Strategies. *J. Mater. Chem.* **2009**, *19*, 2107–2117.
12. Kim, S.-K.; Lee, S. B. Highly Encoded One-Dimensional Nanostructures for Rapid Sensing. *J. Mater. Chem.* **2009**, *19*, 1381–1389.
13. Banholzer, M. J.; Millstone, J. E.; Qin, L.; Mirkin, C. A. Rationally Designed Nanostructures for Surface-Enhanced Raman Spectroscopy. *Chem. Soc. Rev.* **2008**, *37*, 885–897.

14. Banholzer, M. J.; Qin, L.; Millstone, J. E.; Osberg, K. D.; Mirkin, C. A. On-Wire Lithography: Synthesis, Encoding and Biological Applications. *Nat. Protoc.* **2009**, *4*, 838–848.
15. Nam, J.-M.; Thaxton, C. S.; Mirkin, C. A. Nanoparticle-Based Bio-Bar Codes for the Ultrasensitive Detection of Proteins. *Science* **2003**, *301*, 1884–1886.
16. Alivisatos, P. The Use of Nanocrystals in Biological Detection. *Nat. Biotechnol.* **2004**, *22*, 47–52.
17. Qin, L.; Zou, S.; Xue, C.; Atkinson, A.; Schatz, G. C.; Mirkin, C. A. Designing, Fabricating, And Imaging Raman Hot Spots. *Proc. Nat. Acad. Sci. U.S.A.* **2006**, *103*, 13300–13303.
18. Rosi, N. L.; Mirkin, C. A. Nanostructures in Biodiagnostics. *Chem. Rev.* **2005**, *105*, 1547–1562.
19. Cao, Y. C.; Jin, R.; Mirkin, C. A. Nanoparticles with Raman Spectroscopic Fingerprints for DNA and RNA Detection. *Science* **2002**, *297*, 1536–1540.
20. Nicewarner-Pena, S. R.; Freeman, R. G.; Reiss, B. D.; He, L.; Pena, D. J.; Walton, I. D.; Cromer, R.; Keating, C. D.; Natan, M. J. Submicrometer Metallic Barcodes. *Science* **2001**, *294*, 137–41.
21. Tok, J. B.-H.; Chuang, F. Y. S.; Kao, M. C.; Rose, K. A.; Pannu, S. S.; Sha, M. Y.; Chakarova, G.; Penn, S. G.; Dougherty, G. M. Metallic Striped Nanowires as Multiplexed Immunoassay Platforms for Pathogen Detection. *Angew. Chem., Int. Ed.* **2006**, *45*, 6900–6904.
22. Stoermer, R. L.; Cederquist, K. B.; McFarland, S. K.; Sha, M. Y.; Penn, S. G.; Keating, C. D. Coupling Molecular Beacons to Barcoded Metal Nanowires for Multiplexed, Sealed Chamber DNA Bioassays. *J. Am. Chem. Soc.* **2006**, *128*, 16892–16903.
23. Eastman, P. S.; Ruan, W.; Doctolero, M.; Nuttall, R.; de Feo, G.; Park, J. S.; Chu, J. S. F.; Cooke, P.; Gray, J. W.; Li, S.; et al. Qdot Nanobarcodes for Multiplexed Gene Expression Analysis. *Nano Lett.* **2006**, *6*, 1059–1064.
24. Zanardi, P.; Rossi, F. Quantum Information in Superconductors: Noiseless Encoding in a Quantum Dot Array. *Phys. Rev. Lett.* **1998**, *81*, 4752–4755.
25. Gunnarsson, L.; Bjerneld, E. J.; Xu, H.; Petronis, S.; Kasemo, B.; Kall, M. Interparticle Coupling Effects in Nanofabricated Substrates for Surface-Enhanced Raman Scattering. *Appl. Phys. Lett.* **2001**, *78*, 802–804.
26. Han, M.; Gao, X.; Su, J. Z.; Nie, S. Quantum-Dot-Tagged Microbeads for Multiplexed Optical Coding of Biomolecules. *Nat. Biotechnol.* **2001**, *19*, 631–635.
27. Zhang, Y.; Wang, H.; Nie, J.; Zhou, H.; Shen, G.; Yu, R. Mussel-Inspired Fabrication of Encoded Polymer Films for Electrochemical Identification. *Electrochem. Commun.* **2009**, *11*, 1936–1939.
28. Zhang, W.-M.; Hu, J.-S.; Ding, H.-T.; Wan, L.-J.; Song, W.-G. Programmed Fabrication of Bimetallic Nanobarcodes for Miniature Multiplexing Bioanalysis. *Anal. Chem.* **2009**, *81*, 2815–2818.
29. Qin, L.; Park, S.; Huang, L.; Mirkin, C. A. On-Wire Lithography. *Science* **2005**, *309*, 113.
30. Kelly, K. L.; Coronado, E.; Zhao, L. L.; Schatz, G. C. The Optical Properties of Metal Nanoparticles: The Influence of Size, Shape, and Dielectric Environment. *J. Phys. Chem. B.* **2002**, *107*, 668–677.
31. Li, S.; Schatz, G. C., unpublished work, 2010.
32. Li, S.; Schatz, G. C. The Effect of Surface Roughenss on the Extinction Spectra and Electromagnetic Fields around Gold Nanoparticles. *Mater. Res. Soc. Symp. Proc.* **2008**, *1087*, 1087V01−08.
33. Banholzer, M. J.; Li, S.; Ketter, J. B.; Rozkiewicz, D. I.; Schatz, G. C.; Mirkin, C. A. Electrochemical Approach to and the Physical Consequences of Preparing Nanostructures from Gold Nanorods with Smooth Ends. *J. Phys. Chem. C* **2008**, *112*, 15729–15734.
34. Kelly, K. L.; Jensen, T. R.; Lazarides, A. A.; Schatz, G. C. Modeling Metal Nanoparticles Optical Properties. *Met. Nanopart.* **2002**, 89–118.
35. Raether, H. *Surface Plasmons on Smooth and Rough Surfaces and on Gratings*. Springer: New York, 1988.
36. Martin, C. R. Nanomaterials: A Membrane-Based Synthetic Approach. *Science* **1994**, *266*, 1961–1966.
37. Possin, G. E. Forming Very Small Diameter Wires. *Rev. Sci. Instrum.* **1970**, *41*, 772–774.
38. Preston, C. K.; Moskovits, M. J. Optical Characterization of Anodic Aluminum Oxide Films Containing Electrochemically Deposited Metal Particles. 1. Gold in Phosphoric Acid Anodic Aluminum Oxide Films. *J. Phys. Chem.* **1993**, *97*, 8495.